

A Smagorinsky-Lilly turbulence closure for COSMO-LES: Implementation and comparison to ARPS

WOLFGANG LANGHANS¹, JÜRIG SCHMIDLI¹, AND BALAZS SZINTAI^{2*}

¹ *Institute for Atmospheric and Climate Science, ETH Zurich, Switzerland*

² *Federal Office of Meteorology and Climatology MeteoSwiss, Switzerland*

1 Introduction

Large-eddy simulations (LES) are a powerful tool to study atmospheric turbulence such as found in the convective boundary layer (CBL) or in shear-driven flows. LES turbulence closures have commonly been used also in the cloud-modeling community for kilometer-scale simulations of deep convection (e.g., Klemp and Wilhelmson 1978) and therefore attract an even broader range of scientific researchers. In this work a Smagorinsky-Lilly turbulence model is implemented into COSMO and tested for the neutral and the convective boundary layer. For wall-bounded neutral flows the Smagorinsky-Lilly model performs less accurately (Chow et al. 2005; Pope 2000) compared to more sophisticated RANS closures (e.g., elliptic relaxation models), but its computational efficiency and simplicity is of great advantage (Chow et al. 2005).

The implementation into the COSMO code, which has not been originally designed for LES, is described here. Thereafter, the implementation is tested for idealized neutral (NBL) and convective boundary layer (CBL) flows. Our simulations are compared to the ARPS model (see Xue et al. 2000). The latter has frequently been applied in LES studies (e.g., Chow et al. 2005).

2 Implementation

2.1 Smagorinsky-Lilly turbulence model

The Smagorinsky mixing-length model has been designed to simulate the energy transfer from resolved to unresolved scales across an inertial subrange of locally isotropic three-dimensional turbulence. The resolved motions are separated from residual motions by implicit filtering of the governing equations in space. The residual stress-tensor is defined by a linear eddy viscosity model as

$$\overline{u_i u_j} = \underbrace{-2K_M D_{ij}}_{\text{deviatoric}} + \underbrace{\frac{2}{3}e\delta_{ij}}_{\text{isotropic}} \quad D_{ij} = \frac{1}{2} \left(\frac{\partial U_i}{\partial x_j} + \frac{\partial U_j}{\partial x_i} \right) \quad (1)$$

with an eddy viscosity K_M and the filtered (grid-scale) rate of strain D_{ij} . The isotropic part of the stress-tensor related to the subgrid turbulent kinetic energy e is typically small and therefore neglected¹. Smagorinsky's (1963) original proposal has been adapted by Lilly (1962) to include the effects of buoyancy, such that the eddy viscosity is given as

$$K_M = (c_s l_s)^2 \overline{D} \sqrt{\max \left(0, 1 - \frac{\text{Ri}}{\text{Ri}_c} \right)} \quad (2)$$

*Current affiliation: Hungarian Meteorological Service

¹This assumption is also applied in other NWP models such as, e.g., ARPS, WRF, or CM1.

with the characteristic filtered rate of strain $\overline{D} = (2D_{ij}D_{ij})^{1/2}$, the Smagorinsky length scale l_s given by Deardorff's proposal as $l_s = (\Delta x \Delta y \Delta z)^{1/3}$, the Smagorinsky constant c_s , a critical Richardson number Ri_c , and a (deformation) Richardson number

$$Ri = \begin{cases} N_m^2 / \overline{D}^2 & \text{for saturated air} \\ N^2 / \overline{D}^2 & \text{for unsaturated air.} \end{cases} \quad (3)$$

The moist static stability N_m is defined following Durran and Klemp (1982). An option for anisotropic mixing in vertical and horizontal directions has also been implemented. Thereby, two mixing lengths are computed as

$$l_h = (\Delta x \Delta y)^{1/2} \quad l_v = \Delta z \quad (4)$$

and substituted into Eq. (2) to obtain the corresponding eddy viscosities K_M^h and K_M^v .

The characteristic rate of strain can be rewritten as

$$\overline{D}^2 = 2\{D_{11}^2 + D_{22}^2 + D_{33}^2\} + 4\{D_{12}^2 + D_{13}^2 + D_{23}^2\} \quad (5)$$

and the surface stresses are parameterized using the drag laws

$$\overline{uw}_{surf} = -c_D \rho_{surf} \tilde{u} \sqrt{\tilde{u}^2 + \tilde{v}^2} \quad \text{and} \quad \overline{vw}_{surf} = -c_D \rho_{surf} \tilde{v} \sqrt{\tilde{u}^2 + \tilde{v}^2} \quad (6)$$

with the density at the surface ρ_{surf} and tilde indicating parameters on the lowest model level. This shear stress parameterization using horizontal wind speed appears plausible for flows over weakly sloping surfaces, but for steep slopes the shear stress might be better approximated by the slope parallel wind component.

2.2 Numerical implementation

The deformation tensor is computed in `src_slow_tendencies_rk.f90`. Both normal components and vertical shear components are located at mass-points, while D_{12} is computed at the center of each grid-box's corner (see Fig. 1). Then the eddy viscosities for horizontal fluxes are computed at mass-points from Eq. (2) in `src_turbulence.f90`. For isotropic turbulence an interpolation yields the eddy viscosities for vertical mixing located on half-levels. Optionally, e may be diagnosed from the trace of the deformation tensor.

An implicit discretization is used to calculate (most of) the tendencies. This method is also used for the discretization of the vertical flux divergences in the current operational models, e.g., COSMO-2. However, since the implicit solver was implemented along with a 1D turbulence scheme, the Reynolds-stress divergence is incomplete. In more detail, the mixing tendencies M_u^{TD} and M_v^{TD} appearing in the u - and v -equations, respectively, are simplified by the homogeneous boundary layer approximation, as

$$\begin{aligned} M_u^{TD} &= \dots - \frac{1}{\rho} \frac{\partial}{\partial z} \tau_{13} = \dots - \frac{1}{\rho} \frac{\partial}{\partial z} (-\rho 2K_m^v D_{13}) = \dots - \frac{1}{\rho} \frac{\partial}{\partial z} (-\rho K_m^v (\frac{\partial w}{\partial x} + \frac{\partial u}{\partial z})) \\ &\approx \dots - \frac{1}{\rho} \frac{\partial}{\partial z} (-\rho K_m^v \frac{\partial u}{\partial z}) \\ M_v^{TD} &= \dots - \frac{1}{\rho} \frac{\partial}{\partial z} \tau_{23} = \dots - \frac{1}{\rho} \frac{\partial}{\partial z} (-\rho 2K_m^v D_{23}) = \dots - \frac{1}{\rho} \frac{\partial}{\partial z} (-\rho K_m^v (\frac{\partial w}{\partial y} + \frac{\partial v}{\partial z})) \\ &\approx \dots - \frac{1}{\rho} \frac{\partial}{\partial z} (-\rho K_m^v \frac{\partial v}{\partial z}). \end{aligned}$$

Thus, together with the horizontal flux convergences also the missing parts from these tendencies are computed explicitly in `explicit_horizontal_diffusion.f90`. The Reynolds-stresses related to explicit vertical diffusion, given as

$$\tau_{13expl} = -\rho K_m^v \frac{\partial w}{\partial x} \quad \text{and} \quad \tau_{23expl} = -\rho K_m^v \frac{\partial w}{\partial y},$$

are located above the u and v points, respectively, on the model half-levels (see Fig. 1). This splitting of the tendencies into implicit and explicit contributions is problematic at the lowest model level, as the parameterized surface Reynolds-stresses (see above) can not be split. Thus, a zero-gradient lower boundary condition is assumed for the explicit parts of the Reynolds-stresses on the lowest level, such that vertical mixing of u and v results only from the implicit contribution. For all derivatives (deformation, scalar fluxes, flux divergences) metric correction terms may optionally be computed, such that horizontal diffusion can be evaluated in physical space also for sloping model levels.

To ensure numerical stability the horizontal diffusion coefficients are limited by a maximum non-dimensional value of 0.1. This limiter is also applied to the vertical diffusion coefficients used for explicit vertical mixing, but not for the implicit vertical mixing. This threshold is commonly used in mesoscale models (e.g., WRF) and chosen slightly more stringent than the one resulting from linear analysis.

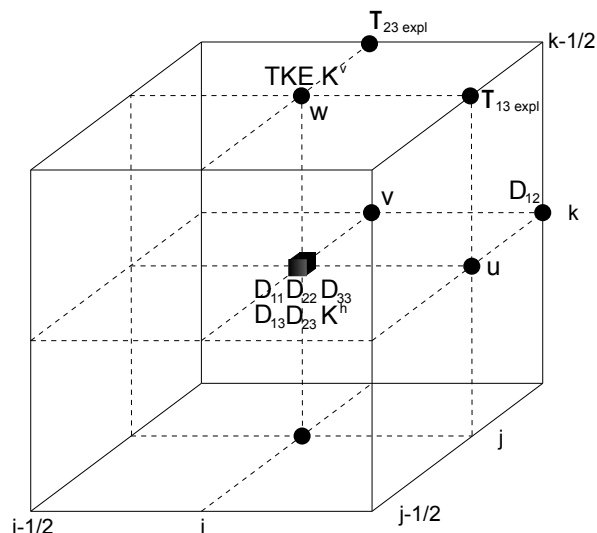


Figure 1: Illustration of the staggering of variables involved within the computation of 3D flux convergences. The mass-point in a grid-box center is indicated by the cube.

3 Simulation of the neutral PBL

The neutral PBL has been intensively studied in the literature (e.g., Andren et al. 1994, Chow et al. 2005, Mirocha et al. 2010). For this type of flow the turbulent scales close to the surface are challengingly small. The forcing is a geostrophic wind in longitudinal-direction driven by a corresponding pressure-gradient. The result for a semi-slip lower boundary condition is a logarithmic wind profile in the surface layer (10-20 % of PBL depth). For a constant eddy viscosity ($K_m^v \neq K_m^v(z)$) the analytical solution of the wind profiles is given by an Ekman-spiral (Stull 1988, pp. 210). The Smagorinsky model is known to over-predict the near-surface stress owing to an under-resolved flow and missing backscatter from the subgrid-scale (Mason and Thompson 1992).

3.1 Model setup

The split-explicit 3rd-order Runge-Kutta time-discretization with explicit 5th-order advection in the horizontal direction and 2nd-order implicit vertical advection is utilized for these simulations. No explicit computational diffusion has been applied. The timestep is 0.125 s, which gives a maximum initial advective Courant number of roughly 0.15. The domain spans $1280 \times 1280 \times 1500$ meters with double periodic lateral boundary conditions. The grid-spacing is $\Delta x = 10$ m in the horizontal directions, while a stretched grid is used in the vertical with a minimum $\Delta z_{min} = 10$ m at the surface and a maximum $\Delta z_{max} = 65$ m at the top. The stretching is given by

$$\Delta z_i = \Delta z_m + \frac{\Delta z_{min} - \Delta z_m}{\tanh(2)} \tanh\left\{\frac{2}{1-a}(i-a)\right\} \quad \text{for } i = 1, ke \quad (7)$$

with $\Delta z_m = 0.5(\Delta z_{min} + \Delta z_{max})$, $a = 0.5(1 + ke)$, and $ke = 40$. The total number of nodes is $129 \times 129 \times 41^2$. A free-slip boundary condition ($\tau_{ij} = 0$, $w = 0$) is applied at the top and the standard dynamic bottom boundary condition is used. The transfer coefficient of momentum c_D is given for a neutral PBL as $c_D = \kappa^2 \ln\{(z_0 + 0.5\Delta z_{min})z_0^{-1}\}^{-2}$ with a surface roughness length $z_0 = 0.1$ m. The transfer of heat is zero. In agreement with Mirocha et al. (2010) we set $c_s = 0.25$ and $Ri_c = 0.7$.

We initialize our simulations with a dry neutral stratification and an Ekman-spiral for a geostrophic wind $u_G = 10 \text{ m s}^{-1}$. The Ekman layer depth equals our domain height. Following the approach of Andren et al. (1994) random perturbations are added to the initial velocities to spin-up a fully-turbulent flow. The maximum magnitude u' of the perturbations decreases from $\pm 0.5 \text{ m s}^{-1}$ at the surface to zero at 700 m. The Coriolis force is applied to perturbations from the geostrophic background flow.

3.2 Results

Inertial oscillations with a time period of $2\pi/f \sim 17$ h are expected before a steady state is reached after ~ 80 hours. Andren et al. (1994) defined non-stationarity parameters with a value of one as soon as the steady-state solution is reached. A time-period of 24 hours is simulated here, since the steady-state solution is not of primary interest. Figures 2a,b demonstrate that COSMO-LES is capable of capturing the frequency of these oscillations.

The turbulence closure itself performs as expected. Coherent structures (see Fig. 2c) appear to be of similar structure as those obtained from WRF simulations (Mirocha et al. 2010). Figure 3a shows the averaged wind profile normalized by the (time-averaged) friction velocity $u_* = 0.41$. Chow et al. (2005) found a similar value of 0.44. The wind shear in the surface layer is overestimated with too strong winds in the upper parts of the surface layer. Also shown is the dimensionless wind shear ϕ (see Fig. 3b), which deviates from the expected value of one in the surface layer. These features are well known and characteristics of the Smagorinsky model (e.g., Mason and Thompson 1992; Chow et al. 2005). The splitting of the Reynolds-stresses and the assumptions made for the lower boundary condition appear to have only minor impacts on the wind speed close to the surface. This is reasonable, since close to the surface the dominating contributions to τ_{13} and τ_{23} are the vertical derivatives of the horizontal velocities. The omitted explicit contributions to the near-surface stress seem to be negligible.

²Note that three grid lines are used for periodic data exchange at each lateral boundary.

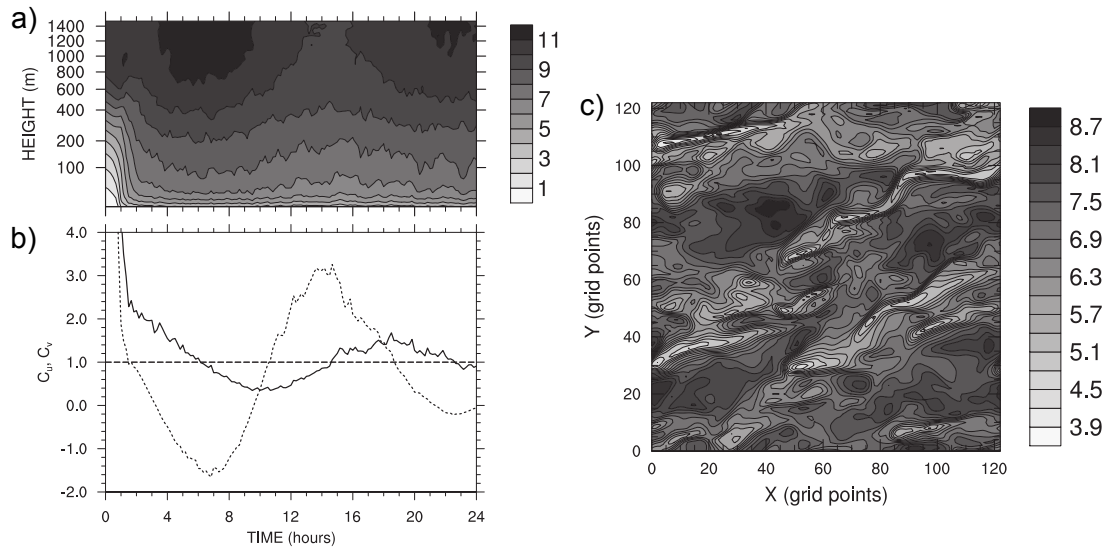


Figure 2: First-order quantities as simulated with COSMO-LES: Time-evolution of (a) mean u -velocity (m s⁻¹) and (b) non-stationarity parameters (solid) C_u and (dashed) C_v and (c) horizontal cross section of u -velocity (m s⁻¹) at 47 meters above ground and after 18 hours. Data output interval in (a,b) is 10 minutes.

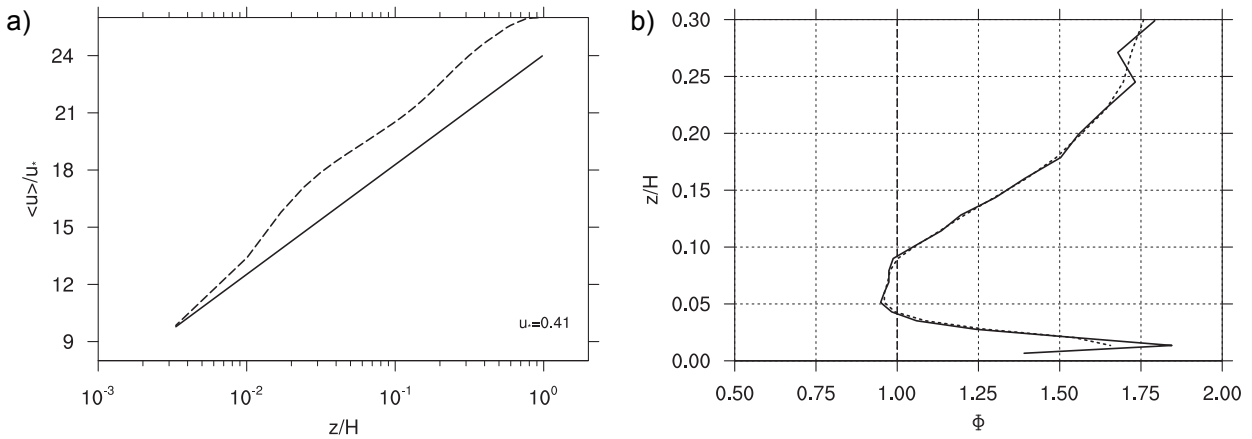


Figure 3: Averaged vertical profiles between 4 and 24 hours: (a) Semi-logarithmic diagram of wind speed normalized by the averaged friction velocity, (b) nondimensional wind shear. The solid line in a) indicates the log-profile obtained from surface layer similarity theory and a 1-2-1 filtered shear profile (dashed curve) has been added in panel b).

4 Simulation of the convective PBL

The convective boundary layer has been the focus of several studies in the past. Nieuwstadt et al. (1993) (abbreviated N93 in the following) shows that LES codes reproduce its characteristics very well. Compared to wall-bounded flows, the characteristic eddy size is determined by the boundary layer depth and can usually be resolved on the grid without the need for excessively small grid-spacings. Moreover, the CBL is less sensitive to the formulation of the lower boundary condition.

4.1 Model setup

The same discretization schemes and boundary conditions are applied as described above. The domain spans 5×5 km² in the horizontal and 2 km in the vertical direction. If not

mentioned otherwise, the grid-spacings have been chosen in agreement with Moeng et al. (2007), who applied equidistant grid-spacings of $\Delta x = 50$ m and $\Delta z = 20$ m, giving $101 \times 101 \times 100$ grid-points³. The large timestep is 0.25 s.

In designing the initial thermodynamic profile we closely follow Moeng et al. (2007) and specify a constant potential temperature of 300 K below $z_{i0} = 1000$ m, a rapid increase by 8 K over an inversion depth of 150 m, and a constant lapse-rate of 3 K km⁻¹ above. Other specifications include the Coriolis parameter $f = 10^{-4}$ s⁻¹, the surface roughness length $z_0 = 0.1$ m, and the critical Richardson (Prandtl) number $Ri_c = 0.46$. The surface sensible heat flux is specified by increasing the surface temperature by 5 K compared to the first level and turbulence is initiated by adding random temperature fluctuations between -0.1 and 0.1 on the lowest four model levels.

Runs with $\Delta x = 25$ m are also conducted. For those runs the time step (number of grid-points) is decreased (increased) in proportion. At both grid-spacings different values of c_s are applied such that both the impact of grid-spacing and the impact of increased subgrid-mixing (at constant grid-spacing) can be analyzed (see Tab. 1). Results are compared to one simulation using ARPS with the same initial and grid specifications. ARPS uses a one-equation mixing-length model, which solves an additional equation for e and relates it to an eddy viscosity. The corresponding Smagorinsky constant c_s would be 0.29 in ARPS. Following Mason and Brown (1999) (abbreviated as MB99 in the following) simulations were run for 10000 s and averaged profiles and spectra were computed over the last 4000 s using a data output interval of 12.5 s (and 60 s for ARPS).

4.2 Results

Simulated statistics of the CBL are presented in Tab. 1. The entrainment flux $\langle w'\theta' \rangle_e$ and the convective velocity scale w_* have been scaled with the actual values of the kinematic surface heat flux Q_s and w_{*0} , respectively, before time-averaging. The entrainment flux of COSMO-LES is slightly stronger than in ARPS. All simulations result in stronger entrainment than in previous LESs (see N93), since a strong temperature inversion at the PBL top is used in our simulations. Thus, the entrainment fluxes are similar to simulations using WRF (Moeng et al. 2007) with the same temperature profile. The spread among the normalized velocity scales w_*/w_{*0} is in agreement with results from several models presented by N93.

Name	l_s (m)	c_s	Δx (m)	z_i (m)	Q_s	$\langle w'\theta' \rangle_e/Q_s$	w_{*0} (m s ⁻¹)	w_*/w_{*0}
50C29	10.7	0.29	50	1049.84	0.1008	-0.2723	1.4874	1.0143
50C32	11.8	0.32	50	1059.07	0.1012	-0.2701	1.4894	1.0165
50C46	17.0	0.46	50	1047.23	0.1040	-0.2418	1.5030	1.0149
25C29	6.7	0.29	25	1061.43	0.1037	-0.2678	1.5016	1.0176
25C46	10.7	0.46	25	1066.23	0.1048	-0.2897	1.5070	1.0172
ARPS	10.7	0.29	50	1101.19	0.1115	-0.2227	1.5385	1.0286

Table 1: Simulation specifications and statistics of the convective boundary layer obtained from COSMO-LES and ARPS for $9 < t/t_* < 15$ (i.e. 321 output values): boundary layer height z_i , surface kinematic heat flux Q_s , scaled entrainment temperature flux $\langle w'\theta' \rangle_e/Q_s$, convective velocity scale w_{*0} , and scaled velocity scale w_*/w_{*0} .

Figures 4a,b show total and subgrid-scale sensible heat flux profiles. A linear decrease of the total heat flux is obtained in all simulations, but the subgrid-mixing results in positive fluxes above the PBL in COSMO-LES. Owing to a slightly higher surface heat flux the boundary

³Again, three grid lines were used for periodic exchange at each lateral boundary.

layer height is marginally higher in ARPS (see also Tab. 1). Although 50C29 and 50C32 produce similar subgrid-fluxes as ARPS near the ground, simulations 50C46, 25C29, and 25C46 result in improved COSMO-LES profiles of the total heat flux near the surface. Using $\Delta x = 25$ m the detrainment of heat at the PBL top is still larger than in ARPS.

Variances of the velocity fluctuations are shown in Figs. 4c,d. The subgrid-scale variance has been computed as $2/3e$, with the subgrid energy e estimated for homogeneous turbulence in equilibrium (see Eq. (7) in Moeng et al. 2007). In general, good agreement with ARPS is achieved. Larger c_s result in reduced total variances. At the PBL top 25C29 results in better agreement of $\langle u'u' \rangle$ with ARPS than 50C29. Such differences in $\langle u'u' \rangle$ have also been found by N93 from different formulations of subgrid-mixing.

Third moments of vertical velocity fluctuations are shown in Figs. 4e,f. Increasing c_s with constant $\Delta x = 50$ m (Fig. 4e) reduces the maximum $\langle w'w'w' \rangle$ such that comparable values are obtained for 50C46 and ARPS. In contrast, 25C46 produces stronger $\langle w'w'w' \rangle$ than 25C29 (Fig. 4f). In general the obtained values of both COSMO-LES and ARPS are higher than those found by N93. In contrast to results presented in previous studies no unphysical negative values are found near the surface.

Total and subgrid temperature variances are shown in Figs. 4g,h. Following N93 the subgrid-scale variance is computed as $0.67^{-4} \langle w'\theta' \rangle^2 e^{-1}$. The profiles agree quite well with ARPS. Only the maximum variance close to the PBL top is larger with COSMO-LES. As indicated by N93 this is a consequence of the increased production of variance related to stronger mean temperature gradients. Indeed, we found higher mean temperature gradients close to the PBL top for COSMO-LES (not shown). Note that in comparison to N93's simulations both models reveal by factor ~ 6 larger $\langle T'T' \rangle$, since a strong temperature inversion is used here at the PBL top.

The effects of grid-spacing and subgrid turbulent length scale are further illustrated in Fig. 5, which shows vertical velocity spectra obtained from all simulations. The spectra have been scaled following MB99. Figure 5 demonstrates that COSMO-LES agrees well with ARPS. Particularly, 50C29, 50C32, and 25C46 reveal very similar spectral distributions to ARPS. In agreement with MB99 the filter scale is determined by the subgrid scheme, since larger c_s (thus larger turbulent length scale) results in stronger filtering for the same numerical grid (see Fig. 5a). Figure 5b shows that, compared to 50C29, 25C29 results in more energy at high frequencies, as the filter scale becomes smaller in 25C29. According to Fig. 5b (and in agreement with MB99) the influence of grid-spacing on simulations with identical turbulent length scale (50C29 vs. 25C46) is small. Note that independently of the distance from the surface COSMO-LES exhibits slightly more energy at the very small scales than ARPS. This is likely related to explicit numerical filtering applied only in ARPS, but not in COSMO-LES.

Finally, Fig. 6 shows horizontal cross-sections of the vertical velocity and the potential temperature fluctuation at $z=110$ m for both 50C29 and ARPS. Both runs produce secondary flows of warm rising air comparable to previous LESs, e.g., Moeng et al. (2007). Distributions from other COSMO-LES runs are shown in Fig. 7. 25C46, which applies the same turbulent length scale as 50C29, but uses a finer grid-spacing, produces similar widths and strengths of the coherent structures. As expected, a larger turbulent length scale (larger c_s) at constant grid-spacing causes enhanced smoothing of the updrafts (25C29 vs. 25C46).

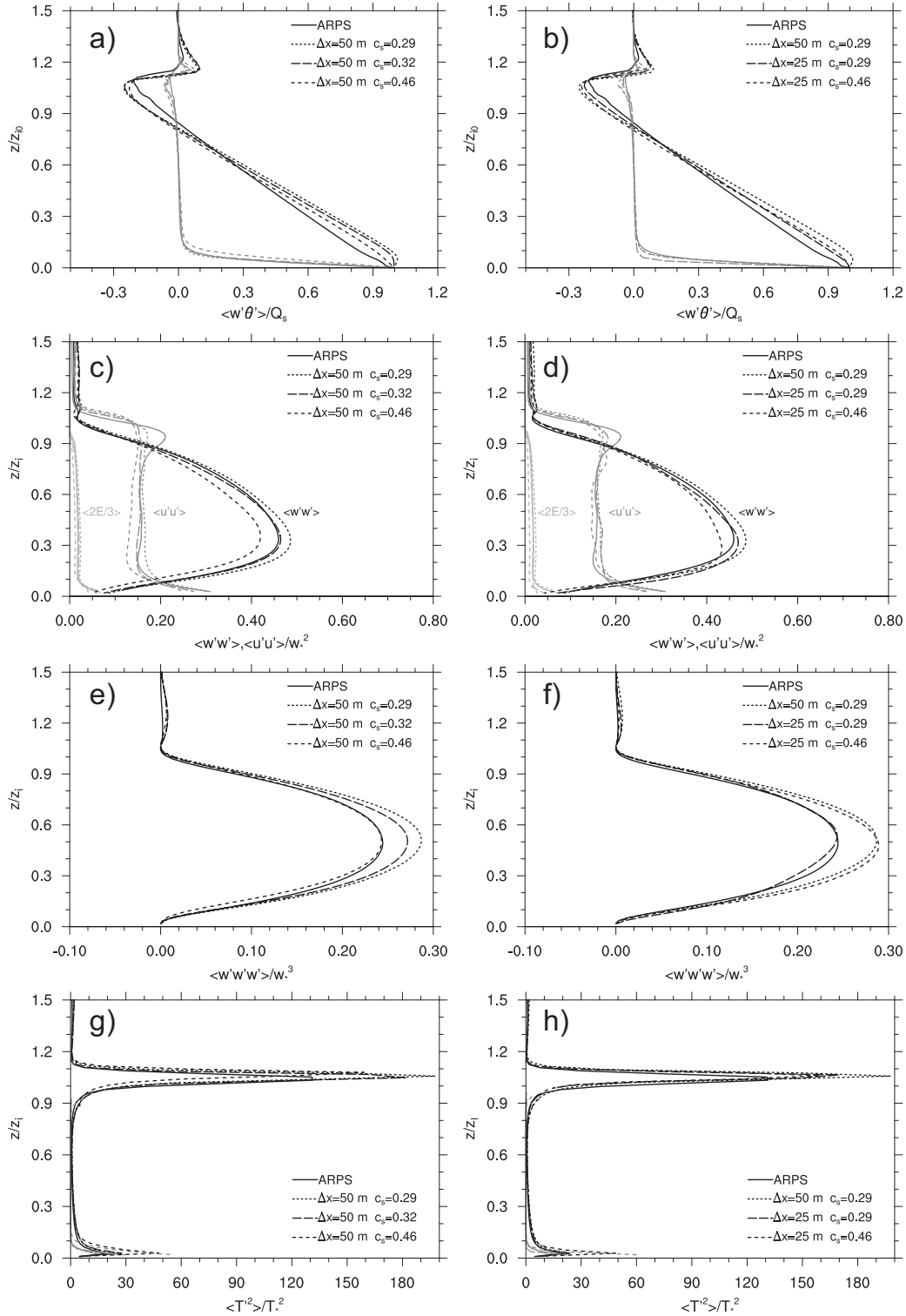


Figure 4: Scaled vertical profiles of domain and time-averaged (a,b) total (black) and subgrid-scale (gray) heat flux, (c,d) w (black), u (dark gray), subgrid-scale (light gray) velocity variances, (e,f) resolved part of third moment of w fluctuations, and (g,h) total (black) and subgrid-scale (gray) temperature variances. Parameters have been scaled by the actual values before averaging. The boundary layer depth z_i is given for each simulation in Tab. 1.

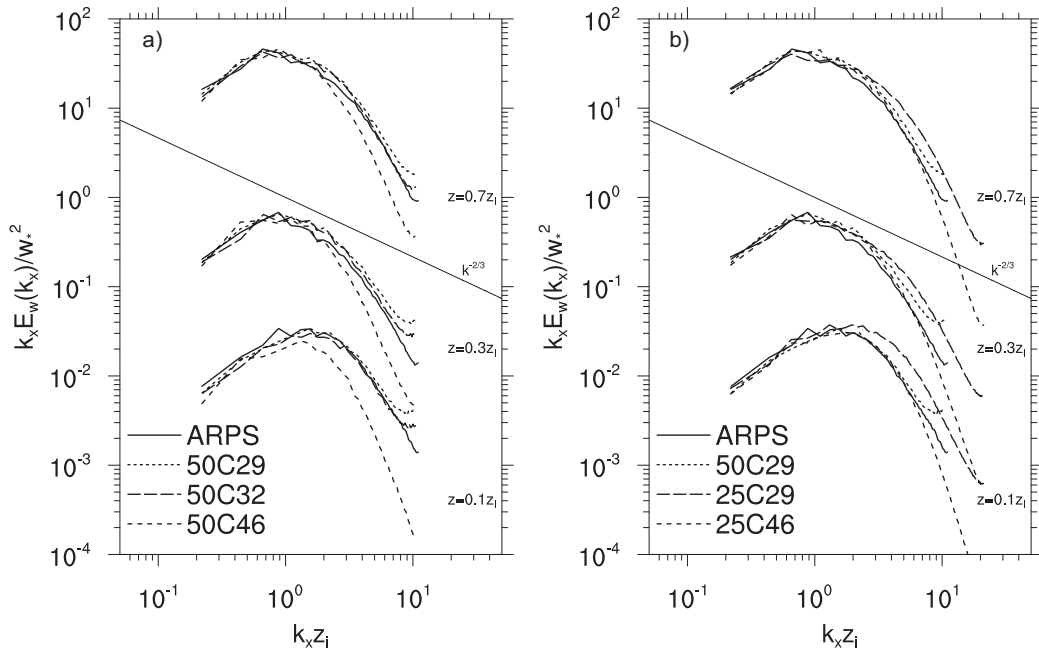


Figure 5: Scaled spectra of vertical velocity at three different levels $0.1z_i$, $0.3z_i$, and $0.7z_i$. Spectra have been computed in x -direction and have been averaged over a time span of 4000 s. The boundary layer depth z_i and velocity scale w_* are both given for each simulation in Tab. 1. Note that the spectral energy has been multiplied by 10 and 1000 at $z = 0.3z_i$ and $z = 0.7z_i$, respectively.

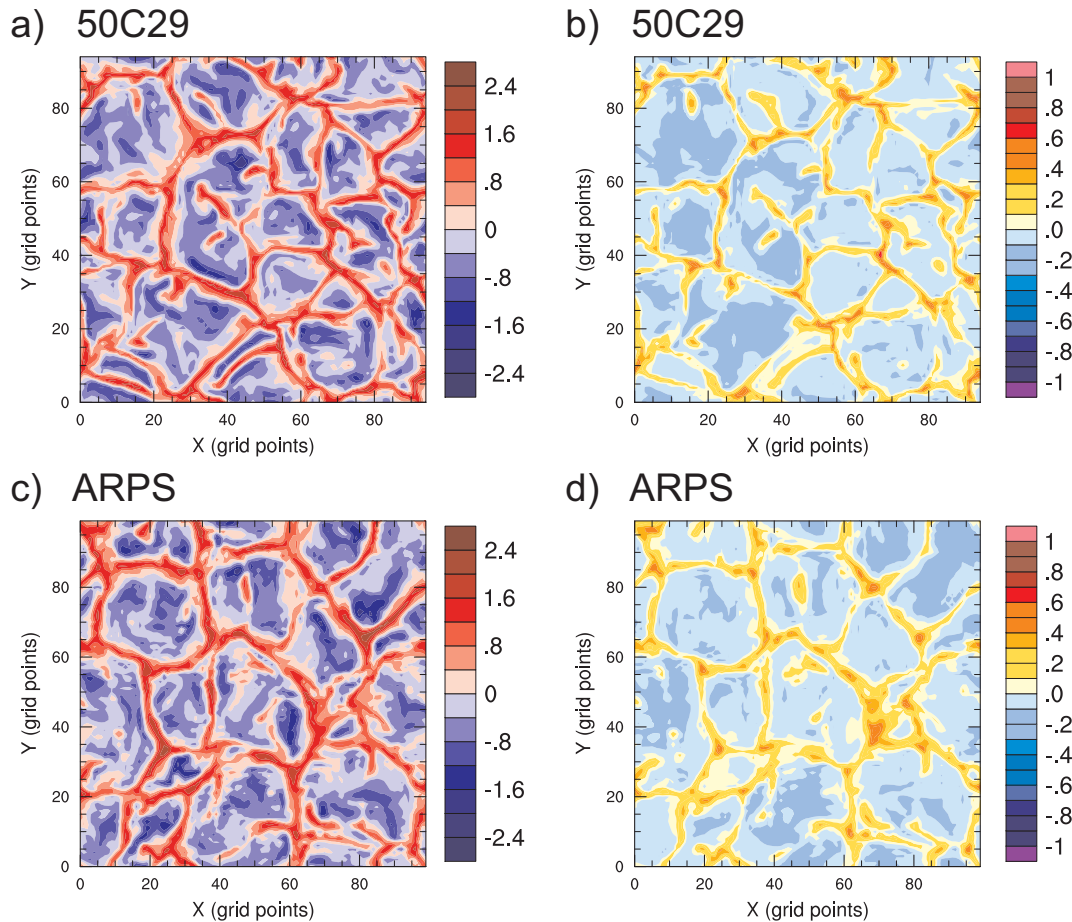


Figure 6: Horizontal cross-sections of (a,c) vertical velocity (m s^{-1}) and (b,d) potential temperature perturbation (K) at $z = 110$ m and after 10000 s from 50C29 and ARPS.

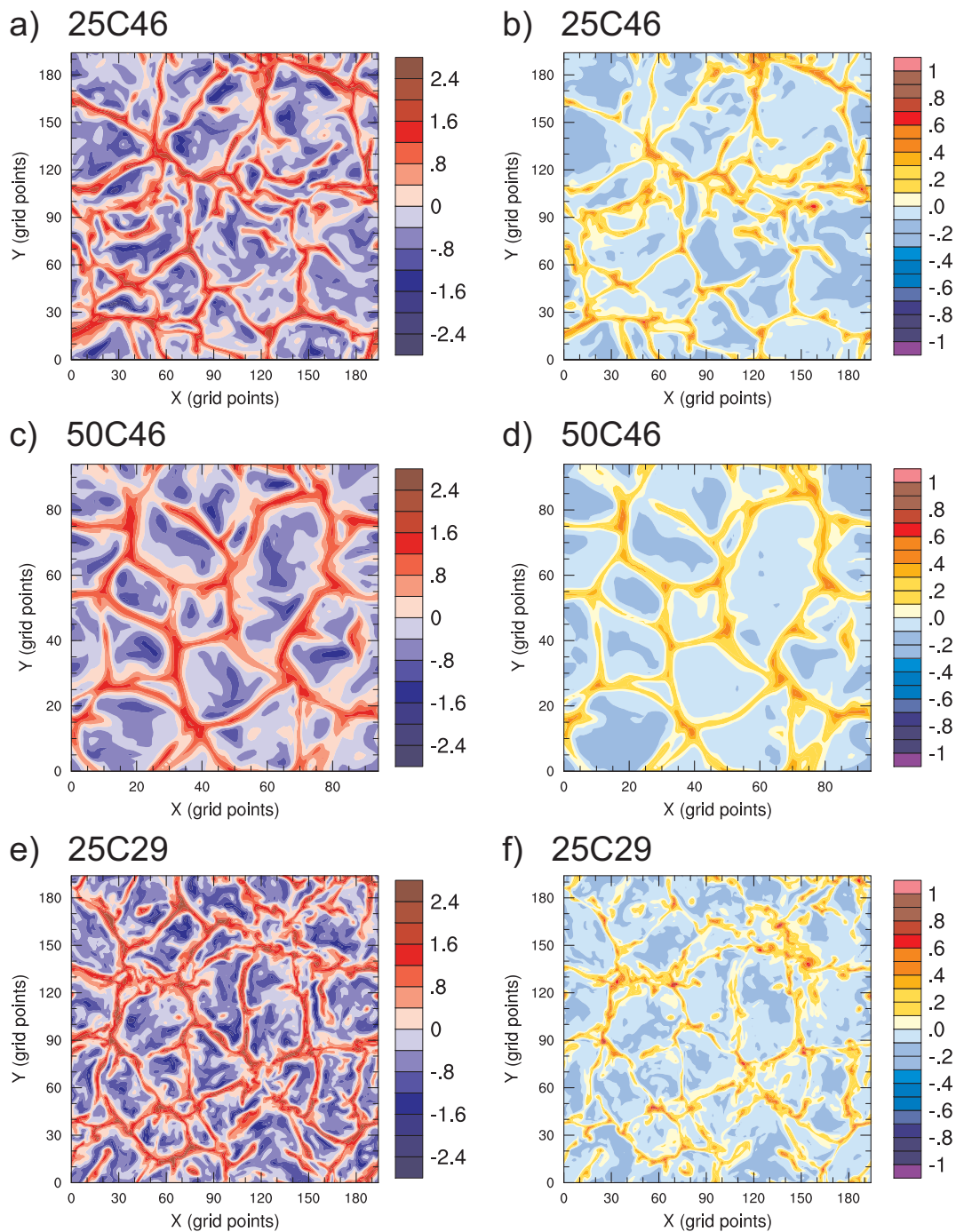


Figure 7: Same as Fig. 6, but from (a,b) 25C46, (c,d) 50C46, and (e,f) 25C29. In 25C46 the same subgrid turbulent length scale l_s is used as in 50C29 (see Fig. 6).

5 Summary and Outlook

A Smagorinsky-Lilly turbulence closure for large-eddy simulations (LES) has been implemented in COSMO. The momentum tendencies had to be split into implicitly and explicitly calculated contributions. Parts of the vertical and all horizontal flux convergences are computed explicitly, while the remaining tendencies from vertical diffusion are solved implicitly. At the lower boundary only the implicitly computed part related to vertical shear of horizontal velocities contributes to the stress. This appears to have little influence on the mean near-surface wind-shear. Simulations of the neutral boundary layer proved that COSMO-LES is capable of reproducing the expected vertical wind-shear as typically obtained from simulations using an eddy viscosity model.

The convective boundary layer as simulated by COSMO-LES has been compared to results obtained with ARPS and to previous studies. A spectral analysis revealed very good agreement of COSMO-LES and ARPS. The simulated vertical profiles of scaled heat flux, velocity and temperature variances, and third moments of the vertical velocity fluctuations demonstrated a general agreement with those references. Only minor deviations to ARPS were found at the very top of the CBL, where larger subgrid-mixing resulted in weak detrainment of heat. Close to the top of the PBL the variances of horizontal velocity were slightly smaller than in ARPS. For smaller grid-spacing ($\Delta x = 25$ m) the variances of horizontal velocity were slightly larger close to the PBL top and the near-surface heat fluxes increased strictly linearly with height.

Future studies would be helpful to address the convergence of COSMO-LES across a larger range of different grid-spacings. A systematic analysis would certainly contribute to an enhanced credibility of COSMO-LES. Although COSMO-LES has also already been used successfully in real-case simulations of deep moist convection, further studies of idealized flows, particularly moist convection, would be helpful to support its credibility to simulate small-scale processes.

References

- [1] Andren, A., A.R. Brown, J. Graf, P.J. Mason, C.-H. Moeng, F.T.M. Nieuwstadt, and U. Schumann, 1994: Large-eddy simulation of a neutrally stratified boundary layer: A comparison of four computer codes. *Quart. J. Roy. Meteor. Soc.*, **120**, 1457-1484.
- [2] Chow, F.K., R.L. Street, M. Xue and J. H. Ferziger, 2005: Explicit filtering and reconstruction turbulence modeling for large-eddy simulation of neutral boundary layer flow. *J. Atmos. Sci.*, **62**, 2058-2077.
- [3] Klemp J.B., R.B. Wilhelmson, 1978: The Simulation of Three-Dimensional Convective Storm Dynamics. *J. Atmos. Sci.*, **35**, 1070-1096.
- [4] Mason, P.J. and D.J. Thompson, 1992: Stochastic backscatter in large-eddy simulations of boundary layers. *J. Fluid Mech.*, **242**, 51-78.
- [5] Mason, P.J. and A. R. Brown, 1999: On subgrid models and filter operations in large eddy simulations. *J. Atmos. Sci.*, **56**, 2101-2114.
- [6] Moeng, C.-H., J. Dudhia, J. Klemp and P. Sullivan, 2007: Examining two-way grid nesting for large-eddy simulation of the PBL using the WRF model. *Mon. Wea. Rev.*, **135**, 2295-2311.

- [7] Mirocha J.D., J.K. Lundquist and B. Kosović, 2010: Implementation of a nonlinear subfilter turbulence stress model for large-eddy simulation in the Advanced Research WRF model. *Mon. Wea. Rev.*, **138**, 4212-4228.
- [8] Nieuwstadt, F.T.M., P.J. Mason, C.-H. Moeng, and U. Schumann, 1993: Large-Eddy simulation of the convective boundary layer: A comparison of four computer codes. *8th Symposium on Turbulent Shear Flows*, Springer-Verlag.
- [9] Pope, S.B., 2000: *Turbulent flows*, Cambridge University Press, pp. 770.
- [10] Xue, M., K. K. Droegemeier, and V. Wong, 2000: The Advanced Regional Prediction System (ARPS) - A multiscale nonhydrostatic atmospheric simulation and prediction tool. Part I: Model dynamics and verification. *Meteor. Atmos. Physics*, **75**, 161-193.